iScience

CellPress
OPEN ACCESS

Article

High C_2-C_4 selectivity in CO_2 hydrogenation by particle size control of Co-Fe alloy nanoparticles wrapped on N-doped graphitic carbon

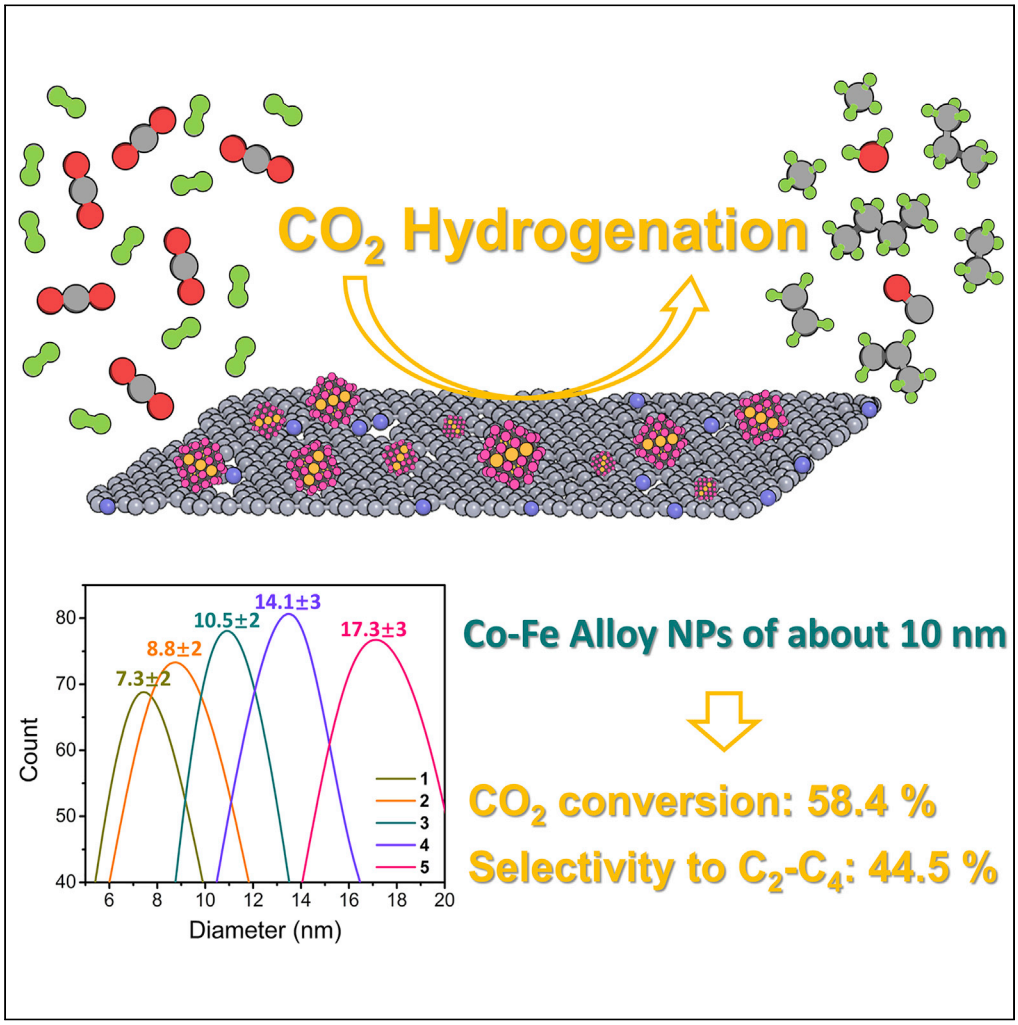

Lu Peng, Bogdan Jurca, Ana Primo, Alvaro Gordillo, Vasile I. Parvulescu, Hermenegildo García

vasile.parvulescu@chimie.unibuc.ro (V.I.P.)
hgarcia@upv.es (H.G.)

Highlights

Co-Fe nanoparticles wrapped on N-doped graphitic carbon catalyzes CO_2 hydrogenation

Co-Fe@(N)Carbon affords 51% selectivity to C_2-C_4 hydrocarbons at 36% CO_2 conversion

At H_2/CO_2 4, 300°C and 5 bar, a combined 30% of CH_2 = CH_2 and MeCH = CH_2 is achieved

Particle size (10 nm) and N-doping are crucial to achieve high C_{2+} selectivity

Peng et al., iScience 25, 104252
May 20, 2022 © 2022 The Author(s).
https://doi.org/10.1016/j.isci.2022.104252

iScience

CellPress
OPEN ACCESS

Article

High C_2-C_4 selectivity in CO_2 hydrogenation by particle size control of Co-Fe alloy nanoparticles wrapped on N-doped graphitic carbon

Lu Peng,[1,4] Bogdan Jurca,[2,4] Ana Primo,[1] Alvaro Gordillo,[3] Vasile I. Parvulescu,[2,*] and Hermenegildo García[1,5,*]

SUMMARY

A catalyst based on first-row Fe and Co with a record of 51% selectivity to C_2-C_4 hydrocarbons at 36% CO_2 conversion is disclosed. The factors responsible for the C_{2+} selectivity are a narrow Co-Fe particle size distribution of about 10 nm and embedment in N-doped graphitic matrix. These hydrogenation catalysts convert CO_2 into C_2-C_4 hydrocarbons, including ethane, propane, *n*-butane, ethylene and propylene together with methane, CO. Selectivity varies depending on the catalyst, CO_2 conversion, and the operation conditions. Operating with an H_2/CO_2 ratio of 4 at 300°C and pressure on 5 bar, a remarkable combined 30% of ethylene and propylene at 34% CO_2 conversion was achieved. The present results open the way to develop an economically attractive process for CO_2 reduction leading to products of higher added value and longer life cycles with a substantial selectivity.

INTRODUCTION

Capture and utilization can be a viable strategy to decrease CO_2 atmospheric emissions, making it possible to reach the objectives for gradual decarbonization (Cuéllar-Franca and Azapagic, 2015). Among the various CO_2 reactions considered, hydrogenation has attracted considerable attention since the products are demanded as fuels and chemicals in a scale commensurate with the CO_2 volumes to be transformed (Yang et al., 2017).

CO_2 hydrogenation can result in different products, compounds with one carbon atom (C_1), such as CH_4 and CO, are the most widely reported (Saeidi et al., 2014). However, from the economic point of view, hydrocarbons with more than one carbon (C_{2+}) are more attractive (Albero et al., 2020) since they can be subsequently transformed into olefins or aromatics. However, while in the Fischer-Tropsch synthesis, a mixture of hydrocarbons with a typical Anderson-Schultz-Flory distribution is generally obtained from CO hydrogenation, in the case of CO_2, the selectivity is strongly biased toward the formation of C_1 products (Wang et al., 2011). Therefore, it is important to develop catalysts of CO_2 hydrogenation with an increased selectivity toward C_{2+} products (Albero et al., 2020; Gao et al., 2018). In the present study, we report that Co-Fe alloy nanoparticles (NPs) of about 10 nm average size wrapped on N-doped graphitic carbon can exhibit selectivity toward C_2, C_3, and C_4 over 50% under optimal conditions at CO_2 conversions over 30%. The catalyst exhibits a remarkable stability, conversion, and selectivity being maintained in 20 h run measurements. The work derives from the systematic study on the influence of the average Co-Fe NP size on the catalytic activity of Co-Fe alloy NPs supported on an N-doped graphitic carbon matrix. In the case of the related CO hydrogenation, there is a window of catalyst particle size that is optimal to achieve higher selectivity (Bezemer et al., 2006; Borg et al., 2008; Den Breejen et al., 2009; Prieto et al., 2009). Although Co and Fe nanoparticles have been widely reported as catalysts for CO_2 hydrogenation, the results presented here prove that by controlling their electron density by strong interaction with the graphitic carbon support and fine-tuning of the particle size distribution, it is possible to drive the selectivity of CO_2 hydrogenation toward C_{2+} products, reaching a combined C_{2+} selectivity among the highest ever reported.

RESULTS AND DISCUSSION

Catalysts preparation and characterization

There is abundant literature showing the activity of Co, Fe, and their alloys as catalysts of CO_2 hydrogenation (Satthawong et al., 2013; Wang et al., 2011). Recently, we also reported that small nanometric clusters

[1]Instituto Universitario de Tecnología Química, Universitat Politècnica de València-Consejo Superior de Investigaciones Científicas, Av. De Los Naranjos s/n, 46022 Valencia, Spain

[2]Department of Organic Chemistry and Biochemistry and Catalysis, Faculty of Chemistry, University of Bucharest, Bdul Regina Elisabeta 4-12, Bucharest 030016, Romania

[3]BASF SE, 67056 Ludwigshafen Am Rhein, Germany

[4]These authors contributed equally

[5]Lead contact

*Correspondence: vasile.parvulescu@chimie.unibuc.ro (V.I.P.), hgarcia@upv.es (H.G.)

https://doi.org/10.1016/j.isci.2022.104252

This is an open access article under the CC BY-NC-ND license (http://creativecommons.org/licenses/by-nc-nd/4.0/).

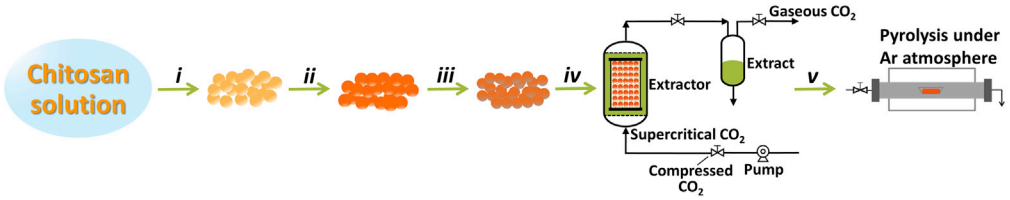

Scheme 1. Procedure used to prepare the Co-FeNPs@(N)G samples under study

(*i*) Formation of chitosan alcogel spheres by precipitation of acid aqueous chitosan solution with NaOH and gradual replacement of H_2O by ethanol.

(*ii*) Impregnation of Co^{2+} and Fe^{2+} salts on chitosan alcogel beads by suspending the microspheres in $CoCl_2$-$FeCl_2$-ethanol solution.

(*iii*) Formation of metal alloy NPs performed by reduction with $NaBH_4$.

(*iv*) Supercritical CO_2 drying.

(*v*) Pyrolysis at 900°C under Ar atmosphere.

of Co-Fe alloy NPs supported on graphitic carbon at low total metal content (<0.2 wt %) is a highly selective catalyst for reverse water gas shift reaction, promoting the conversion of CO_2 to CO with a selectivity over 98%, accompanied by minor percentages of CH_4 (Peng et al., 2021). On the other hand, catalysts with a broad particle size distribution of Co-Fe alloys on N-doped graphene afford CH_4 selectively. Those studies showed that, although single Co and Fe metals are also active, the best activity is obtained for Co-Fe alloys. This is in accordance with previous studies in the literature (Sandupatla et al., 2019; Satthawong et al., 2013; Stowe and Russell, 1954; Wang et al., 2011).

What has not been disclosed is the control of CO_2 hydrogenation selectivity toward C_{2+} products. It will be shown that a remarkable C_{2+} selectivity can be achieved by controlling the particle size of Co-Fe alloy NPs supported on N-doped graphitic carbon. Five samples, 1–5, were prepared following exactly the same preparation procedure that affords a narrow particle size distribution, but increasing the total metal loading from 9 to 23 wt %. The preparation method is sketched in Scheme 1, while Table 1 summarizes the main analytical data of the samples under study. The Co and Fe content in the samples used as catalysts was determined by ICP-AES analysis after dissolving the metals in the samples with *aqua regia*, while combustion chemical analysis allows quantification of N and C. The N content of the five samples was similar, around 1.5 wt % (see Table 1).

As it can be seen in Scheme 1, the precursor of the graphitic carbon is chitosan, a homopolymer of glucosamine obtained by deacetylation of natural chitin, the main waste of the fishery industry (Hamed et al., 2016; Khanafari et al., 2008; Salaberria et al., 2015). Chitosan, containing N and C in its composition, acts simultaneously as a source of C and N forming turbostratic N-doped graphitic carbon (Candu et al., 2019; Hao et al., 2015; Lavorato et al., 2014; Primo et al., 2014). One of the known properties of chitosan is to adsorb a large percentage of metal salts from solution due to the complexation of the metal ions with chitosan functional groups and the formation of numerous strong hydrogen bridges (Vakili et al., 2019; Wang and Zhuang, 2017; Wu et al., 2010). In the present case, millimetric alcogel beads of chitosan, formed by flocculation of acid chitosan aqueous solution with NaOH and gradual replacement from H_2O to ethanol, were impregnated with a mixture of $CoCl_2$-$FeCl_2$ in ethanolic solution. After impregnation, the formation of metal alloy NPs was performed by reduction with $NaBH_4$. Subsequent supercritical CO_2 drying and final pyrolysis render the Co-FeNPs@(N)G catalysts. A crucial step in the preparation of the catalysts with narrow particle size distribution is the $NaBH_4$ reduction, since analogous samples prepared following the same procedure, but without the $NaBH_4$ reduction step, result in a sample with a broad particle size from 5 to over 50 nm. Apparently, formation of small metal NPs by chemical reduction with $NaBH_4$ before pyrolysis is responsible for a better particle size control and less atomic mobility than if the starting precursor sample contains isolated metal ions undergoing chemical reduction at high temperatures. Regarding the life cycle assessment, it should be commented that the catalyst preparation procedure indicated in Scheme 1 based on pyrolysis should emit CO_2 evolved from the polysaccharide decomposition and the energy consumption required in the pyrolysis, without counting the CO_2 footprint of Co and Fe mining. However, turnover cycles of the catalyst should make the impact of catalyst preparation to the overall CO_2–footprint balance of the process not relevant.

All recorded XRD patterns present well-defined reflections, with a signal-to-noise ratio suitable for Rietveld analysis (Figures 1A and S1). The refinement process gave good reliability factors. All fresh samples 1–5

Table 1. List of samples under study and their main analytical data and average particle size

Sample no.	Co (wt %)[a]	Fe (wt %)[a]	Total Co + Fe content (wt %)[a]	C (wt %)[b]	N (wt %)[b]	Average particle size (nm)[c]	Particle size distribution (nm)[d]
1	7.9	1.6	9.5	74.3	1.9	7.3	5.5–9.7
2	14.0	3.5	17.5	69.6	1.6	8.8	6.5–11.0
3	14.1	3.5	17.6	63.5	1.4	10.5	8.5–13.2
4	17.2	4.0	21.3	64.5	1.7	14.1	10.4–16.3
5	19.2	4.1	23.3	57.1	1.3	17.3	14.1–21.8

[a]Determined by ICP-AES analysis after dissolving the metals in *aqua regia*. *The error of the analysis is 0.1%.*
[b]It is assumed that the rest to 100% is residual oxygen.
[c]Determined by DF-TEM.
[d]Plotted in Figure 2K.

present only two metal-containing cubic crystalline phases: fcc (space group Fm-3m) and bcc (Im-3m); the only exception is catalyst 4 for which a reflection located around $2\theta = 40.4°$ (matching the JCPDS card #49-1720 of a C_{60} phase) has been considered to originate from the carbonaceous support and, thus, it was excluded from the Rietveld refinement (Figure S1D).

In all catalyst samples (fresh and spent), Rietveld refinement indicates that the samples are Co-Fe alloys. The fit underestimates the fcc (111) reflection (located at $2\theta \sim 44°$) intensity, whereas the intensity of the (200) reflection ($2\theta \sim 51.2°$) is obviously overestimated. Such a situation is a clear indication of a preferred orientation effect toward [111] direction. Indeed, taking into consideration the correction modeled by the March-Dollase formalism, the quality of the fit improved, leading to subunitary R_0 coefficients (Table S1) that are typical for plate-shaped crystals. The (111) section of the fcc structure is a honeycomb lattice of points separated by distances of ~2.50 Å ($a\sqrt{(2)}/2$), close to 2.46 Å ($\sqrt{(3)} \cdot d_{C-C}$); $d_{C-C} \simeq 1.42$ Å) which is the distance between the voids (*i.e.* empty centers of the hexagons) of a two-dimensional graphite/graphene sheet. It is proposed that such a geometric match would therefore induce the preferential [111] growth of metallic fcc nanoparticles on the graphene support. No preferred orientation effects could be put in evidence for the bcc phase ($R_0 = 1$).

The Co/Fe content of all catalyst samples slightly varies around 80% mole fraction of Co; for this composition, the Co-Fe phase diagram (Wang et al., 2017) indicates three possible solid phases (in temperature increasing order): an ordered bcc (CsCl-like structure stabilized by Co-Fe magnetic interactions), a disordered bcc (antisite defects rather than vacancies (Neumayer and Fähnle, 2001), followed by the fcc phase. The ease of transitions between the phases depends mainly on the atomic Co/Fe ratio: for the equiatomic $Co_{0.5}Fe_{0.5}$ composition, heating at 550°C for 52 h and slow cooling promotes ordering, whereas further room temperature ball milling at 500 rpm for up to 150 min promoted disorder (Loureiro et al., 2011). For deviations from the equiatomic Co/Fe composition, as those of the present samples 1–5, the difficulty for the phase transitions to occur increases significantly: bulk $Co_{0.8}Fe_{0.2}$ needs ~50 h at 700°C to achieve ordering or ~500 h at 400°C (Ohnuma et al., 2002). For all our catalysts, the annealing treatment performed under Ar for 2 h at 900°C determines the formation of the fcc and a single bcc phase (Figure S1) most likely disordered, due to the short extent of the thermal treatment. Moreover, this short thermal treatment is not likely to transform a significant amount of bcc Co-Fe alloy by ordering phase transitions toward fcc, but the direct formation of this phase is probably correlated with the geometrical match between the [111] direction of the Co-Fe alloy and the graphene support. On the other hand, the evolution of the amount of bcc and fcc phases from fresh to spent catalysts (Table S1 and Figure S1) can also not be explained solely by the role of the temperature (1.5 h dwells from 300°C to 500°C with 50°C steps), too low and for too short time to induce phase transitions. It is more likely that the observed evolution is determined by exposure of the small metallic nanoparticles to substrates and products in the catalytic reaction.

The structural parameters obtained from the Rietveld analysis of the XRD patters matches very well the data obtained from HRTEM observations: the bcc phase of catalyst sample 3 (fresh) has a unit cell parameter $a = 2.8419 \pm 0.0002$ Å for which an interplanar distance $d_{111} = 2.0095 \pm 0.0001$ Å is obtained, very close to $d_{111} = 2.01$ Å (Figure 3). The textural analysis based on the size- and strain-broadening of the reflection profiles offers an estimation of the average extent of coherently scattering domains; the obtained

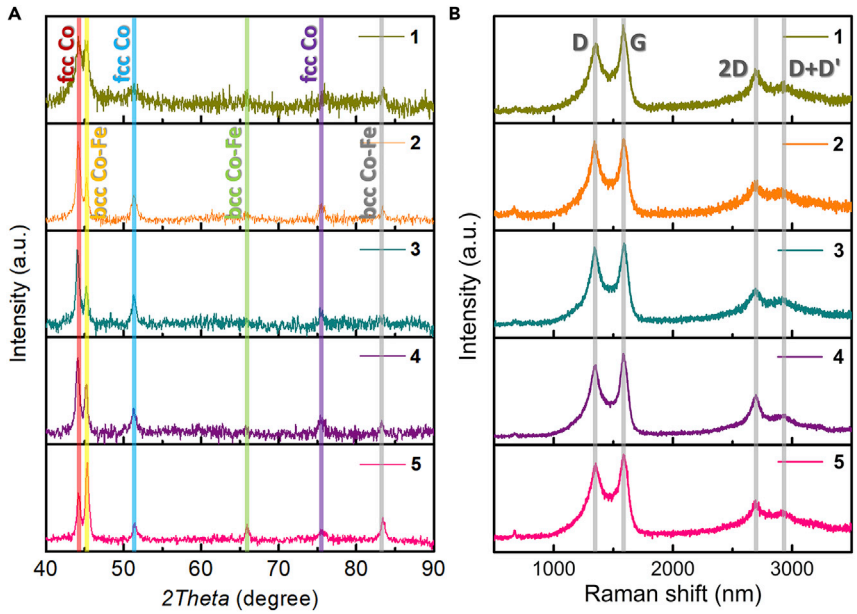

Figure 1. XRD patterns (A) and Raman spectra (B) of the samples 1–5 as indicated in the plot

(A) Red, blue, and purple straight lines refer to (111), (200), and (220) planes of Co fcc phase (JCPDS #15-0806), respectively. Yellow, green, and gray straight lines refer to (110), (200), and (211) planes of $Co_{0.7}Fe_{0.3}$ bcc phase (JCPDS #48-1818), respectively.

(B) The gray straight lines from left to right represent D, G, 2D, and D + D′ bands located at 1350, 1590, 2700, and 2960 cm^{-1}.

values of the particle size compared with DF-TEM results are in satisfactory (fresh catalysts 1 and 2) or good (catalysts 3 to 5) concordance.

Raman spectroscopy was coincident for all the samples and very similar to those reported turbostratic graphitic carbon residues derived from chitosan pyrolysis (Lavorato et al., 2014; Primo et al., 2014). The presence of the D + D′, 2D, G, and D bands appearing at 2960, 2700, 1590, and 1350 cm^{-1}, respectively, was recorded with a relative intensity of the G over the D band of 1.15. This indicates that the samples are constituted by defective graphene sheets with a quality similar to that of reduced graphenes. Figure 1 presents the XRD patterns and Raman spectra of samples 1–5.

Field emission scanning electron microscopy (FESEM) images of samples 1–5 were very similar showing a spongy, highly porous carbon residue without any hint of metal particles at the micrometric scale. Selected FESEM images of the materials are provided in Figure S2. In accordance with the morphology revealed by FESEM, the specific surface area of sample 3 obtained by isothermal N_2 adsorption/desorption measurements is 384 m^2/g and the total pore volume is 0.75 cm^3/g. The information provided by transmission electron microscopy (TEM) was very relevant to understand the nature and size of the metal nanoparticles. Thus, in the dark-field (DF) mode, TEM images reveal that the samples are constituted by NPs, accompanied, with a bright background that corresponds to dispersed metal clusters of size below the detection limit of the TEM instrument. Figure 2 provides selected images. Statistical determination of the particle size indicates that a major parameter controlling the average particle size is the total metal loading on the support. The composition of the graphitic carbon is also important, since it influences the metal-support interaction. Thus, although samples 2 and 3 have almost coincident metal loading, they have somewhat different average particle size due to differences in the carbon and oxygen content of the graphitic matrix. In this way, following the procedure indicated in Scheme 1, Co-Fe@(N)C samples with narrow particle size distribution from 7 to 17 nm could be prepared (see Table 1). This tendency of larger particle size as the loading increases is well established in the literature for supported metal NPs (Wang and Chen, 1991; Zhu and Zaera, 2014). Importantly, the particle size distribution was notably narrow, particularly in comparison of analogous samples prepared omitting the $NaBH_4$ reduction step. Figure S3 provides TEM images of the sample prepared without reduction. Again, the use of $NaBH_4$ to obtain metal NPs with narrow particle

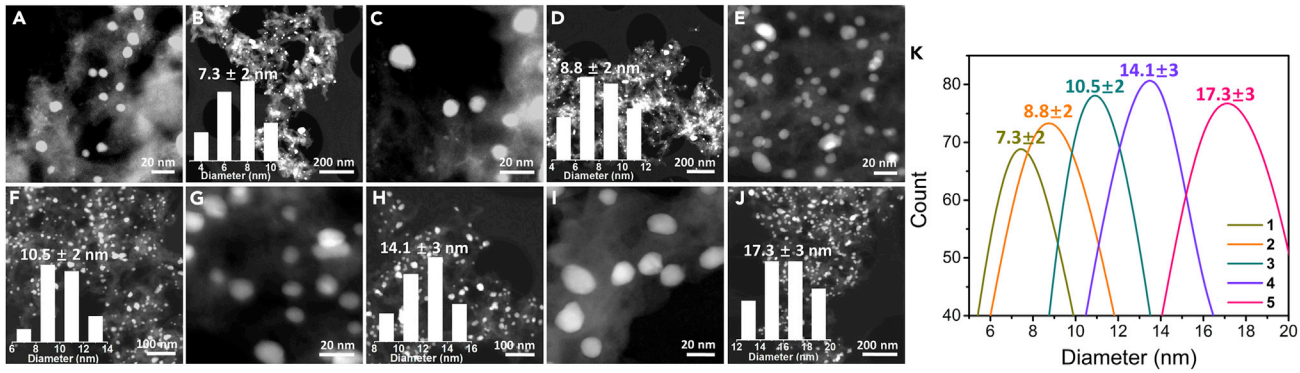

Figure 2. DF-TEM images (A–J) and particle size distribution diagram (K) of samples 1–5

(A, B) sample **1**.

(C, D) sample **2**.

(E, F) sample **3**.

(G, H) sample **4**.

(I, J) sample **5**.

size distribution is well established in the literature (Cookson, 2012; Liu et al., 2012; Mavani and Shah, 2013; Zhao and Friedrich, 2017). It seems that preformed metal NPs do not tend to evolve during the pyrolysis step into a broad size distribution, probably due to the interaction during the thermal treatment either with the chitosan fibrils or with the N-doped graphitic carbon derived therefrom.

High-resolution TEM images also give two other crucial information. Measurement of the interplanar distance of 2.01 Å corresponding to the 110 plane indicates that the NPs are constituted by random Co-Fe alloy with no evidence of independent Co or Fe NPs. Energy dispersive spectrometry (EDS) elemental mapping (Figure S4) of the Co-Fe NPs by TEM also indicates a spatial coincidence of Co and Fe in the NPs. The second information is that the Co-Fe NPs surrounded by the graphitic carbon matrix are wrapped by a few layers of N-doped graphene, observing a large interfacial contact between the two components. Figure 3 presents images providing support to the above claims of random alloying between Co and Fe and the wrapping of the Co-Fe NPs by a few graphene layers.

Catalytic activity

Reactions were carried out in a pressurized stainless steel tubular reactor at temperatures between 300°C and 500°C. After activation at 300°C under N_2, each catalyst was submitted to a 5 h test starting at 300°C and increasing the temperature in 50°C steps. Each temperature is maintained for 1 h. Analysis of the reaction products was carried out on line with multichannel gas chromatography (GC) that quantifies the percentage of CO_2, CO, CH_4, and C_{2+} products. Data at each temperature correspond to the average value of the analysis measured for each temperature at 30, 45, and 55 min. Controls in the absence of any catalyst or using N-doped graphitic residue prepared as indicated in Scheme 1, but in the absence of Co or Fe metals, show a CO_2 conversion at 400°C of 0.3% and 2.5%, respectively, methane, being the only product detected in these blank tests.

With the purpose of finding a relationship between product distribution, and particularly C-C bond formation, and particle size of Co-Fe nanoparticles, the activity of samples 1–5 was studied. When samples 1–5 were used as catalysts, besides the formation of CH_4 as the main product, the formation of CO and C_2-C_4 hydrocarbons was also observed in variable proportions, depending on the catalyst and reaction conditions. In the distribution of C_2-C_4 products, ethane was always the major component, followed by propane and lesser amounts of *n*-butane. In addition, the presence of ethylene (major) and propylene (minor) was also detectable. Figure S5 and Tables S2–S6 contain full analytic data of the reaction for each catalyst, at each temperature and condition screened in the present work. As an example, Figure 4 presents CO_2 conversion and product distribution for samples 1–5 as catalysts measured at 400°C working at 10 bar with an H_2/CO_2 ratio of 7 and a space velocity of 6000 h^{-1}. As it can be seen there, the percentage of CO decreases, while the proportion of CH_4 increases in general with the particle size.

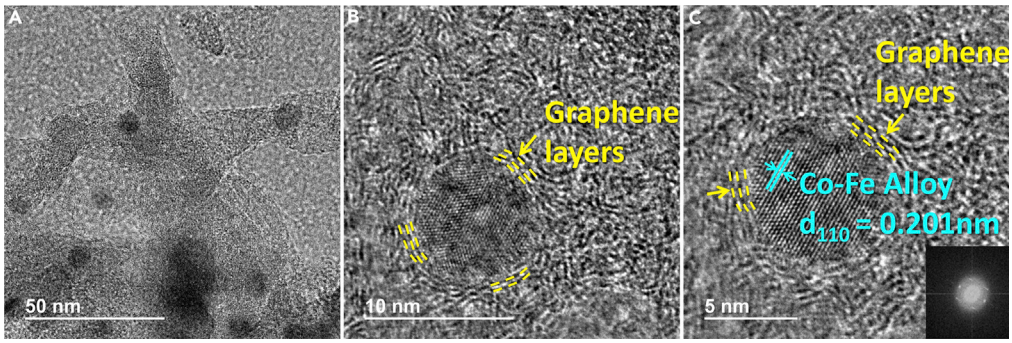

Figure 3. TEM images at three different magnifications of sample 3 (A, B and C correspond to scale bars of 50, 10 and 5 nm, respectively).

The interplanar distance for the Co-Fe alloy nanoparticle measured by HRTEM is indicated in image C that also indicates the graphene layers with yellow arrows. The inset in image C corresponds to the Fast Fourier transformed (FFT) electron diffraction of the particle showing that it corresponds to a single crystal of Co-Fe alloy NP.

General trends were observed in the activity of samples 1–5 as CO_2 hydrogenation catalysts. Conversion of CO_2 increases with temperature, particularly in the range from 300°C to 450°C, while the increase from 450°C to 500°C is less notable. Product selectivity depends on the catalyst, CO_2 conversion, and operation conditions, including temperature, H_2/CO_2 ratio, and pressure. Caution should be taken when comparing the selectivity values at different conversions among the various catalysts since in the present case, selectivity depends on conversion.

Commenting on the unique catalytic behavior of samples 1–5, the most salient observation is the formation of a notable percentage of C_{2+} products. A comparison with an analogous Co-Fe sample embedded in N-doped graphitic carbon at the same total metal loading and Co/Fe ratio, but exhibiting a broad particle size distribution shows the selective formation of CH_4 under the same conditions. This control sample was prepared by pyrolysis of $CoCl_2$ and $FeCl_2$ adsorbed on chitosan without the $NaBH_4$ reduction step. Similarly, samples of Co-Fe clusters supported on N-doped graphitic carbon exhibit over 98% CO selectivity at high conversions (Peng et al., 2021).

Besides particle size distribution, the influence of N-doping of the graphitic carbon embedding the Co-Fe nanoparticles on the catalytic performance was studied by preparing an analogous Co-Fe sample using as precursor of the graphitic matrix alginic acid that does not contain N in its composition. After pyrolysis at 900°C under Ar, the resulting Co-Fe@C contains 8.9 and 3.8 wt % of Co and Fe, respectively. The average particle size was 8.0 nm. Figure S6 in supporting information presents CO_2 conversion and product distribution at 10 bar with an H_2/CO_2 ratio of 7 measured at different temperatures for Co-Fe@C that is an analogous catalyst to 1–5, but without N. As it can be seen in Figure S6, CO_2 conversion increased evidently with the temperature. Importantly, in the range of 350°C to 500°C, the main product using Co-Fe@C was methane with a selectivity constantly over 97%, which is different from the catalytic performance of samples 1–5 containing N. Therefore, the selectivity for C_2-C_4 products of samples 1–5 containing N was all higher than that of Co-Fe@C lacking N doping.

Regarding the influence of temperature, it was a general trend that the combined C_{2+} selectivity increased and then decreased with the temperature, reaching maximum selectivity values at intermediate temperatures of 400°C or 450°C (Figure S5). Because CO selectivity decreases with temperature, CH_4 selectivity for all samples 1–5 was maximum at 500°C.

From the catalytic data, it was concluded that samples 3 and 4 were those exhibiting the highest selectivity to C_{2+} at the highest conversion. Because the metal loading and the average Co-Fe particle size were lower for sample 3 than for sample 4 (see Table 1), sample 3 was selected for further stability test and optimization of the C_{2+} selectivity.

The stability of the catalytic activity of sample 3 was assessed performing four consecutives 5 h runs at 10 bar, H_2/CO_2 ratio of 7, and 6000 h^{-1} space velocity. Note that this stability test submits the catalyst

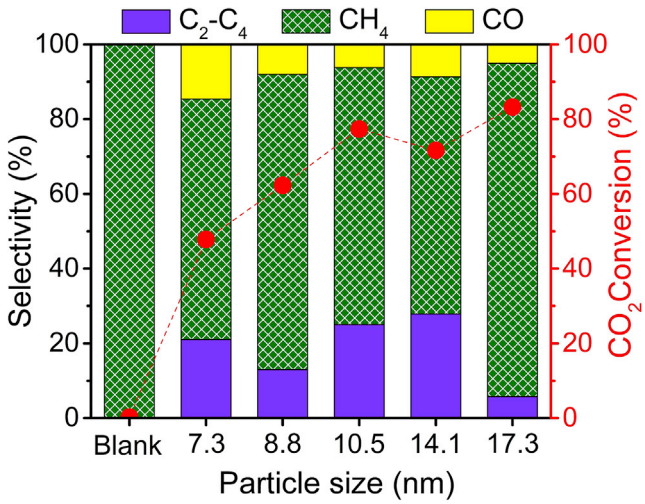

Figure 4. CO_2 conversion and selectivity for samples 1–5 having different particle sizes at 400°C, under the same conditions

Conversion is presented as red dots (right scale) and selectivity for samples 1–5 with different particle sizes is indicated in color codes. Reaction condition: H_2/CO_2 ratio of 7, total flow 4 mL/min, 10 bar, 40 mg catalyst.

to temperature changes every 1 h interval. These fluctuations in the temperature with heating and cooling periods are unfavorable for catalyst stability, since it can lead to deposition of byproducts and reconstruction of metal nanoparticles. Therefore, the stability test conditions of the present study are harder to maintain reproducible conversion and selectivity to the various products than keeping constant the operation parameters. Figure 5 and Table S7 show the results of this stability test. It was observed that catalyst **3** was stable with reproducible conversion and selectivity values at each temperature in cycles 2, 3, and 4. It was also noted, however, that particularly at lower temperatures of 300°C and 350°C, the used sample **3** outperforms CO_2 conversion and C_{2+} selectivity values measured for the fresh sample. This improvement in the performance has also been reported for clusters of Co-Fe supported on N-doped graphitic carbon (Peng et al., 2021) and it has been attributed to surface modification of the Co-Fe particles by partial oxidation due to CO_2 during the first stages of the test and the effect is more noticeable at low temperatures. However, it is worth noting that reproducibility based on the activity data in the temperature range from 400°C to 500°C, in which CO_2 conversion is getting higher, for the four cycles was remarkable. The accumulated turnover number of catalyst **3** in the four uses considering the total metal content is over 200, ensuring that the impact of catalyst preparation in the overall CO_2-footprint of the process is negative.

Having confirmed catalyst stability, the reaction conditions were optimized to achieve the maximum selectivity for C_{2+}. Thus, the influence of the H_2/CO_2 ratio was studied in the range from 7 to 1. A general tendency to decrease CO_2 conversion, while increasing C_{2+} selectivity, upon decreasing the H_2/CO_2 ratio was observed. Figure S7 and Tables S8–S11 contain the full set of catalytic data. A good compromise between conversion and C_{2+} selectivity was achieved at H_2/CO_2 ratios of 3 and 4, for which a CO_2 conversion of 51% with a C_{2+} selectivity of 36% was measured at a temperature of 400°C (H_2/CO_2 ratio of 3) or 350°C (H_2/CO_2 ratio of 4). The best result corresponds to a CO_2 conversion of 34% and a combined C_{2+} selectivity of 51.9%. The activity of sample 3 is markedly higher than that of most active Fe or Co-based catalysts and even ruthenium, nickel, or molybdenum-based catalysts found in the literature. Table S12 summarizes the selectivity for C_2-C_4 hydrocarbons reported in previous studies on CO_2 hydrogenation (Baddour et al., 2020; Cored et al., 2019; Jiang et al., 2018; Kim et al., 2020; Liu et al., 2018; Mutschler et al., 2018; Wang et al., 2018; Yan et al., 2019; Zhao et al., 2021).

Further optimization of C_{2+} selectivity for sample 3 was carried out by varying the reaction pressure from 5 to 40bar. Figure 6 summarizes the results at 300°C for an H_2/CO_2 ratio of 4. The full activity data are also provided in the Supporting Information, Figures S7, S8, and S9 and Tables S13–S24. Evidently, a good balance between CO_2 conversion that increases with the reaction pressure and C_{2+} selectivity was found at 300°C and 40 bar, for which a CO_2 conversion of 58% with a C_{2+} selectivity of 44% was achieved (see Figure 6). Under these conditions, the percentage of ethane, propane, and *n*-butane were 17%, 14%, and 10%,

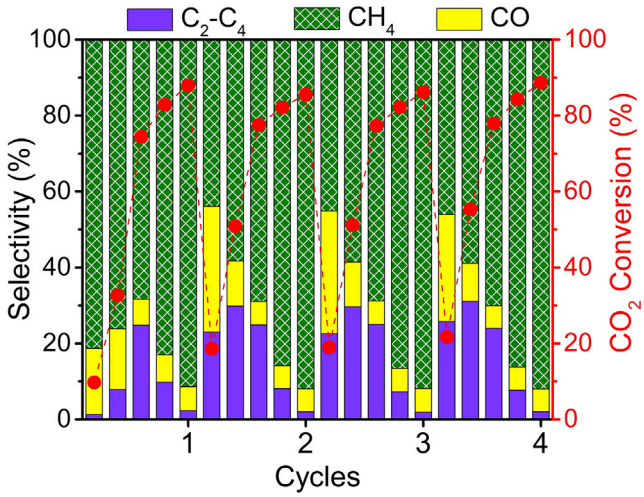

Figure 5. Stability test of sample 3 in four consecutive cycles in which the temperature starts from 300°C to 500°C and increasing in 50°C each step

Conversion is presented as red dots (right scale) and selectivity at each temperature is indicated in color codes. Reaction condition: H_2/CO_2 ratio of 7, total flow 4 mL/min, 10 bar, 40 mg catalyst.

values that are absolutely remarkable for CO_2 hydrogenation. Similar pressure optimization was also carried out for 2 and 1 H_2/CO_2 ratio (Figures S9 and S10) and although C_{2+} selectivity values as high as 61% were achieved with the percentage of CH_3-CH_3 almost 4 times higher than that of CH_4 for 1 H_2/CO_2 ratio at 300°C and 15 bar, CO_2 conversion was barely 22%, as shown in Figure S10B.

Of note is that under these H_2 lean conditions and low pressure, selectivity values of ethylene and propylene as high as 30% were measured at CO_2 conversion over 34% (see Figure S8A, performing at an H_2/CO_2 ratio of 4, 300°C, and 5 bar). Something that could be expected and hints to alkenes as being involved in the reaction mechanism. It should be noted, however, that CO_2 conversion under the present conditions is limited by the space velocity and higher CO_2 conversion values could be easily reached by employing higher amounts of catalyst or diminishing the flow rate.

Theoretical calculations

In order to shed some light on the origin of the high C_{2+} selectivity and the role of graphene as support of bimetallic NPs in the activation of CO_2, DFT calculations were carried out at PBE-D3/def2-SVP level of theory. Models of 20 atoms with a composition $Co_{14}Fe_6$ similar to that of catalyst 3 was used in the study. An initial random geometry was optimized both in the absence and upon interacting with a graphene sheet.

The dissociation and hydrogenation steps of CO_2 on the surface of bimetallic catalysts have been recently studied from a theoretical point of view (Nie et al., 2019). In the present calculations, a similar CO_2 dissociation process has been adopted. However, this precedent has not studied the possible role of graphene as support. Our experimental data indicate that the role of graphene supporting NPs should be significant regarding the activity of bimetallic catalysts based on the TEM images (Figure 3). For this reason, we have first focused our attention on differences of CO_2 adsorption on Co-Fe alloys when they become supported on graphene. Information from molecular electrostatic potential (MEP) surface analysis of non-supported (M1) and supported (G1) Co-Fe cluster model reveals two extremely positive [+34 eV (M1)] and negative [-22 eV (M1)] regions which become much attenuated [+14 and −18 eV (G1)] when the Co-Fe NP is interacting with graphene (Figure 7A). Overall, it is easy to foresee that positive regions (blue color) should be repulsive for CO_2 [δ^+(C) = 0.30] adsorption, whereas strong adsorption should be expected for negative regions (red color), even though highly negative regions do not assist the subsequent desorption process (Zhao et al., 2021). Therefore, it is suggested that the catalysis takes place in the boundary between the afore-mentioned negative and positive regions. Importantly, a key finding of the analysis of the electrostatic potential map comparing M1 and G1 is the change from +1 to −1 eV calculated for the Co atoms of the Co-Fe model far from the graphene support (see arrows in Figure 7A), a fact that reveals the influence of graphene interaction modifying the electronic density of the Co-Fe cluster and, therefore, its adsorption with CO_2.

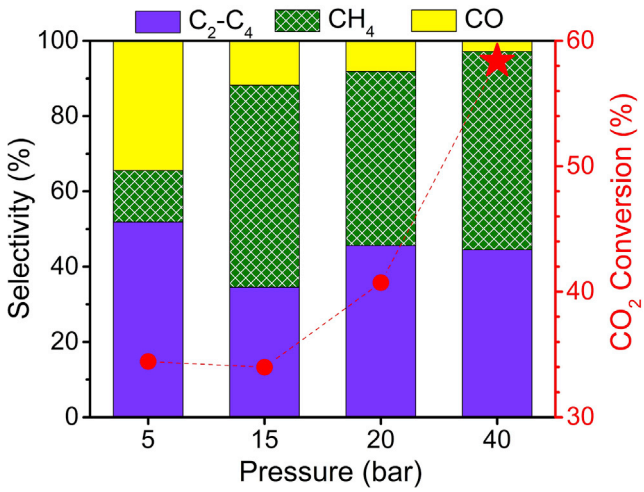

Figure 6. CO_2 conversion and selectivity for sample 3 at 300°C and different pressures

Conversion is presented as red dots (right scale) and selectivity at each pressure is indicated in color codes. Reaction conditions: H_2/CO_2 ratio of 4, total flow 4 mL/min, 40 mg catalyst.

Using these preliminary considerations as a starting point, information about CO_2 dissociation was obtained from the interaction of these model clusters with CO_2 gas. CO_2 adsorption was estimated to be favorable in both model clusters ($E_{ads,\ CO2}$ = −1.7 and −2.1 eV for M1 and G1, respectively), being the most favorable the graphene supported cluster. Then, as proposed in the literature (Nie et al., 2019), dissociation and hydrogenation of CO_2 should take place and evolve toward a metal carbide (-CH_2-) on the metallic surface (Davis, 2001). Carbide species for the clusters supported on graphene (G1 = CH_2) are stabilized (3.8 eV compared to M1 = CH_2) acting as a precursor for the production of desorbed methane (1.9 eV is theoretically required for this production) or C_{2+} products, depending on whether G1 = CH_2 reacts with H_2 or with an adsorbed C_1 intermediate.

It is envisioned that the production of ethylene (C_2H_4) or its hydrogenated product (C_2H_6) should proceed through the insertion of the metal carbene to previously formed CO or methane, a well-known mechanism (Doyle et al., 2010). In fact, the study of this process provides information about the role of metallic atoms. In supported model G1 = CH_2 (Figure 7B), carbon is preferably coordinated on Co atoms, whereas iron activates the C-H bond of carbide and this activation induces a lengthening of this C-H bond about 0.11 Å (from 1.11 to 1.22 Å).

Desorption of ethane (C_2H_6) from the surface proved to be less favorable (+0.4 eV from coordinated species) in comparison to methane. Subsequent production of higher hydrocarbons than C_2 should similarly proceed through C-H activation since G1 = C_2H_4 intermediate on the surface still contain an "active" metal carbide for insertion reactions. In fact, a lengthening of 0.08 Å for the C-H bond was also observed, although this activation is weaker compared to G1 = CH_2 (Figure 7B).

Overall, the present calculations suggest that it is the higher stability of the metal carbenes when the Co-Fe clusters are supported on graphene and their modified electronic distribution is the key factor favoring the chain growth in the present Co-FeNPs@(N)G catalysts as compared to unsupported clusters.

CONCLUSIONS

In summary, the present study has shown the importance of size control in Co-Fe NPs wrapped on N-doped graphitic carbon to favor C-C bond formation during CO_2 hydrogenation. There is a size window around 10 nm of the Co-Fe particle size that favors the formation of C_2-C_4 hydrocarbons and in this regard, CO_2 hydrogenation follows the trend known in Fischer-Tropsch synthesis for which catalysts with a particle size about 10 nm are most adequate to promote the formation of longer-chain hydrocarbons. Small Co-Fe nanoparticles particles promote CO formation, while a broad particle size distribution enhances CH_4 selectivity. Theoretical calculations indicate that graphene as the support strongly modifies the electronic density on the Co-Fe cluster and the C-C bond formation has been ascribed to the higher stability of the

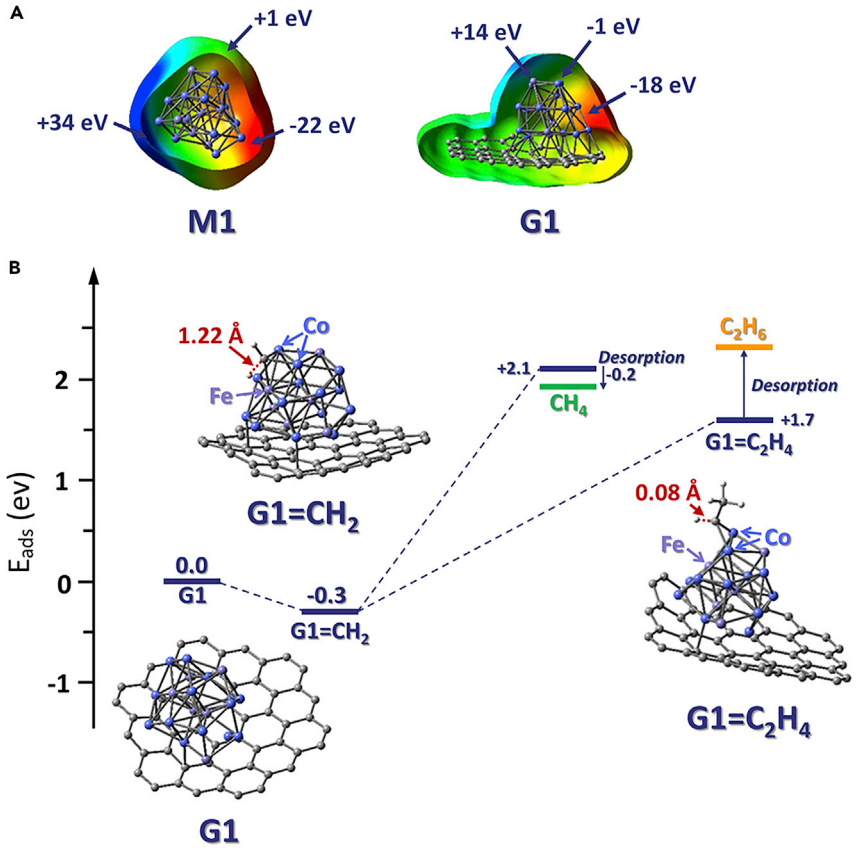

Figure 7. Molecular electrostatic potential surface analysis (A) and optimized structures of hydrocarbons (B)

(A) Molecular electrostatic potential plotted on the van der Waals surface of models for supported (model G1) and unsupported $Co_{14}Fe_6$ alloy (model M1) model.

(B) Optimized structures for methane and ethane precursors at PBE-D3 functional and def2-SVP basis set. Activation of C-H bonds is highlighted by red dashed lines.

Co=CH_2 carbene when the cluster is supported on graphene. To the best of our knowledge about Co- or Fe-based catalysts, the high C_2-C_4 selectivity values reached with the present Co-Fe NP wrapped on N-doped graphitic carbons have no precedent in CO_2 hydrogenation, with C_{2+} selectivity values over 50% and ethylene and propylene selectivity over 30% with a stable catalyst. The selectivity of these products can be useful to increase the economic attractiveness of the process at large scale.

LIMITATIONS OF THE STUDY

Product selectivity depends on the operating conditions and on the catalyst particle size and composition. Similar catalysts can lead to different product distribution favoring the formation of CH_4. The present results have been reproduced with five independent batches in the same catalytic reactor.

STAR★METHODS

Detailed methods are provided in the online version of this paper and include the following:

- KEY RESOURCES TABLE
- RESOURCE AVAILABILITY
  - Lead contact
  - Materials availability
  - Data and code availability
- METHOD DETAILS
  - Materials
  - Synthesis of Co-FeNPs@(N)G

- Characterization of catalysts
- Catalytic tests
- Theoretical calculations

SUPPLEMENTAL INFORMATION

Supplemental information can be found online at https://doi.org/10.1016/j.isci.2022.104252.

ACKNOWLEDGMENTS

Financial support by the Spanish Ministry of Science and Innovation (Severo Ochoa and RTI2018-98237-CO2-R1) and Generalitat Valenciana (Prometeo 2021/38) is gratefully acknowledged. Partial funding by BASF is thankfully acknowledged. V.I.P. thanks UEFISCDI ((PN-III-P4-ID-PCE-2016-0146, 121/2017 and PN-III-P4-ID-PCE-2020-1532) for funding.

AUTHOR CONTRIBUTIONS

L.P. prepared and characterized the Co-FeNPs@(N)G catalysts under the supervision of A.P. B.J. performed the catalytic tests under the supervision of V.I.P. A.G. provided the industrial expertise, driving the research. V.I.P. and H.G. wrote the manuscript with the contribution of all the authors. All the authors revised the manuscript.

DECLARATION OF INTERESTS

Dr. Alvaro Gordillo is an employee of BASF. The study was partially funded by BASF. Hermenegildo Garcia has as second affiliation the Center of Excellence in Advanced Materials Research of the King Abdulaziz University at Jeddah, Saudi Arabia. Vasile I. Parvulescu and Hermenegildo Garcia are inventors of a European patent protecting intellectual property of the present catalysts.

Received: November 3, 2021
Revised: February 15, 2022
Accepted: April 7, 2022
Published: May 20, 2022

REFERENCES

Ahlrichs, R., Bär, M., Häser, M., Horn, H., and Kölmel, C. (1989). Electronic structure calculations on workstation computers: the program system turbomole. Chem. Phys. Lett. *162*, 165–169.

Albero, J., Peng, Y., and García, H. (2020). Photocatalytic CO_2 reduction to C_{2+} products. ACS Catal. *10*, 5734–5749.

Baddour, F.G., Roberts, E.J., To, A.T., Wang, L., Habas, S.E., Ruddy, D.A., Bedford, N.M., Wright, J., Nash, C.P., Schaidle, J.A., et al. (2020). An exceptionally mild and scalable solution-phase synthesis of molybdenum carbide nanoparticles for thermocatalytic CO_2 hydrogenation. J. Am. Chem. Soc. *142*, 1010–1019.

Balzar, D., Audebrand, N., Daymond, M., Fitch, A., Hewat, A., Langford, J., Le Bail, A., Louër, D., Masson, O., and McCowan, C.N. (2004). Size-strain line-broadening analysis of the ceria round-robin sample. J. Appl. Crystallogr. *37*, 911–924.

Bezemer, G.L., Bitter, J.H., Kuipers, H.P., Oosterbeek, H., Holewijn, J.E., Xu, X., Kapteijn, F., van Dillen, A.J., and de Jong, K.P. (2006). Cobalt particle size effects in the Fischer-Tropsch reaction studied with carbon nanofiber supported catalysts. J. Am. Chem. Soc. *128*, 3956–3964.

Borg, Ø., Dietzel, P.D., Spjelkavik, A.I., Tveten, E.Z., Walmsley, J.C., Diplas, S., Eri, S., Holmen, A., and Rytter, E. (2008). Fischer-Tropsch synthesis: cobalt particle size and support effects on intrinsic activity and product distribution. J. Catal. *259*, 161–164.

Candu, N., Man, I., Simion, A., Cojocaru, B., Coman, S.M., Bucur, C., Primo, A., Garcia, H., and Parvulescu, V.I. (2019). Nitrogen-doped graphene as metal free basic catalyst for coupling reactions. J. Catal. *376*, 238–247.

Cookson, J. (2012). The preparation of palladium nanoparticles. Platinum Met. Rev. *56*, 83–98.

Cored, J., Garcia-Ortiz, A., Iborra, S., Climent, M.J., Liu, L., Chuang, C.H., Chan, T.S., Escudero, C., Concepcion, P., and Corma, A. (2019). Hydrothermal synthesis of ruthenium nanoparticles with a metallic core and a ruthenium carbide shell for low-temperature activation of CO_2 to methane. J. Am. Chem. Soc. *141*, 19304–19311.

Cuéllar-Franca, R.M., and Azapagic, A. (2015). Carbon capture, storage and utilisation technologies: a critical analysis and comparison of their life cycle environmental impacts. J. CO_2 Utilization *9*, 82–102.

Davis, B.H. (2001). Fischer-Tropsch synthesis: current mechanism and futuristic needs. Fuel Process. Technology *71*, 157–166.

Den Breejen, J., Radstake, P., Bezemer, G., Bitter, J., Frøseth, V., Holmen, A., and de Jong, K.d. (2009). On the origin of the cobalt particle size effects in Fischer-Tropsch catalysis. J. Am. Chem. Soc. *131*, 7197–7203.

Dollase, W. (1986). Correction of intensities for preferred orientation in powder diffractometry: application of the March model. J. Appl. Crystallogr. *19*, 267–272.

Doyle, M.P., Duffy, R., Ratnikov, M., and Zhou, L. (2010). Catalytic carbene insertion into C-H bonds. Chem. Rev. *110*, 704–724.

Finger, L., Cox, D., and Jephcoat, A. (1994). A correction for powder diffraction peak asymmetry due to axial divergence. J. Appl. Crystallogr. *27*, 892–900.

Frisch, M., Trucks, G., Schlegel, H., Scuseria, G., Robb, M., Cheeseman, J., Scalmani, G., Barone, V., Petersson, G., and Nakatsuji, H. (2016). Gaussian 16 Revision a. 03. 2016, *2* (Gaussian Inc).

Gao, Y., Liu, S., Zhao, Z., Tao, H., and Sun, Z. (2018). Heterogeneous catalysis of CO_2 hydrogenation to C_{2+} products. Acta Physico-Chimica Sinica *34*, 858–872.

Grimme, S., Antony, J., Ehrlich, S., and Krieg, H. (2010). A consistent and accurate ab initio parametrization of density functional dispersion correction (DFT-D) for the 94 elements H-Pu. J. Chem. Phys. *132*, 154104.

Hamed, I., Özogul, F., and Regenstein, J.M. (2016). Industrial applications of crustacean by-products (chitin, chitosan, and chitooligosaccharides): a review. Trends Food Sci. Technology *48*, 40–50.

Hao, P., Zhao, Z., Leng, Y., Tian, J., Sang, Y., Boughton, R.I., Wong, C., Liu, H., and Yang, B. (2015). Graphene-based nitrogen self-doped hierarchical porous carbon aerogels derived from chitosan for high performance supercapacitors. Nano Energy *15*, 9–23.

Jiang, F., Liu, B., Geng, S., Xu, Y., and Liu, X. (2018). Hydrogenation of CO_2 into hydrocarbons: enhanced catalytic activity over Fe-based Fischer-Tropsch catalysts. Catal. Sci. Technology *8*, 4097–4107.

Khanafari, A., Marandi, R., and SANATI, S. (2008). Recovery of Chitin and Chitosan from Shrimp Waste by Chemical and Microbial Methods.

Kim, K.Y., Lee, H., Noh, W.Y., Shin, J., Han, S.J., Kim, S.K., An, K., and Lee, J.S. (2020). Cobalt ferrite nanoparticles to form a catalytic Co-Fe alloy carbide phase for selective CO_2 hydrogenation to light olefins. ACS Catal. *10*, 8660–8671.

Larson, A.C., and Von Dreele, R.B. (1994). Gsas. Rep. lAUR, 86–748.

Lavorato, C., Primo, A., Molinari, R., and Garcia, H. (2014). N-doped graphene derived from biomass as a visible-light photocatalyst for hydrogen generation from water/methanol mixtures. Chemistry-A Eur. J. *20*, 187–194.

Liu, L., Puga, A.V., Cored, J., Concepción, P., Pérez-Dieste, V., García, H., and Corma, A. (2018). Sunlight-assisted hydrogenation of CO_2 into ethanol and C_{2+} hydrocarbons by sodium-promoted Co@C nanocomposites. Appl. Catal. B Environ. *235*, 186–196.

Liu, Q.-m., Zhou, D.-b., Yamamoto, Y., Ichino, R., and Okido, M. (2012). Preparation of Cu nanoparticles with $NaBH_4$ by aqueous reduction method. Trans. Nonferrous Met. Soc. China *22*, 117–123.

Loureiro, J., Batista, A., Khomchenko, V., Costa, B., and Le Caër, G. (2011). Order-disorder phenomena from X-ray diffraction in FeCo alloys annealed and ground at high energy. Powder Diffraction *26*, 267–272.

Mavani, K., and Shah, M. (2013). Synthesis of silver nanoparticles by using sodium borohydride as a reducing agent. Int. J. Eng. Res. Technology *2*, 1–5.

Mutschler, R., Moioli, E., Luo, W., Gallandat, N., and Züttel, A. (2018). CO_2 hydrogenation reaction over pristine Fe, Co, Ni, Cu and Al_2O_3 supported Ru: comparison and determination of the activation energies. J. Catal. *366*, 139–149.

Neumayer, M., and Fähnle, M. (2001). Atomic defects in FeCo: stabilization of the B2 structure by magnetism. Phys. Rev. B *64*, 132102.

Nie, X., Wang, H., Liang, Z., Yu, Z., Zhang, J., Janik, M.J., Guo, X., and Song, C. (2019). Comparative computational study of CO_2 dissociation and hydrogenation over Fe-M (M= Pd, Ni, Co) bimetallic catalysts: the effect of surface metal content. J. CO_2 Utilization *29*, 179–195.

Ohnuma, I., Enoki, H., Ikeda, O., Kainuma, R., Ohtani, H., Sundman, B., and Ishida, K. (2002). Phase equilibria in the Fe-Co binary system. Acta Materialia *50*, 379–393.

Peng, L., Jurca, B., Primo, a., Gordillo, A., Parvulescu, V., and Garcia, H. (2021). Co-Fe clusters supported on N-doped graphene as highly-selective catalysts for reverse water gas shift. ACS Sustainable Chem. Eng. *9*, 9264–9272.

Perdew, J.P., Burke, K., and Ernzerhof, M. (1996). Generalized gradient approximation made simple. Phys. Rev. Lett. *77*, 3865.

Prieto, G., Martínez, A., Concepción, P., and Moreno-Tost, R. (2009). Cobalt particle size effects in Fischer-Tropsch synthesis: structural and in situ spectroscopic characterisation on reverse micelle-synthesised Co/ITQ-2 model catalysts. J. Catal. *266*, 129–144.

Primo, A., Sánchez, E., Delgado, J.M., and García, H. (2014). High-yield production of N-doped graphitic platelets by aqueous exfoliation of pyrolyzed chitosan. Carbon *68*, 777–783.

Saeidi, S., Amin, N.A.S., and Rahimpour, M.R. (2014). Hydrogenation of CO_2 to value-added products-A review and potential future developments. J. CO_2 Utilization *5*, 66–81.

Salaberria, A.M., Diaz, R.H., Labidi, J., and Fernandes, S.C. (2015). Preparing valuable renewable nanocomposite films based exclusively on oceanic biomass-Chitin nanofillers and chitosan. Reactive Funct. Polym. *89*, 31–39.

Sandupatla, A.S., Banerjee, A., and Deo, G. (2019). Optimizing CO_2 hydrogenation to methane over CoFe bimetallic catalyst: experimental and density functional theory studies. Appl. Surf. Sci. *485*, 441–449.

Satthawong, R., Koizumi, N., Song, C., and Prasassarakich, P. (2013). Bimetallic Fe-Co catalysts for CO_2 hydrogenation to higher hydrocarbons. J. CO_2 Utilization *3*, 102–106.

Stowe, R.A., and Russell, W.W. (1954). Cobalt, iron and some of their alloys as catalysts for the hydrogenation of carbon dioxide. J. Am. Chem. Soc. *76*, 319–323.

Thompson, P., Cox, D., and Hastings, J. (1987). Rietveld refinement of Debye–Scherrer synchrotron X-ray data from Al_2O_3. J. Appl. Crystallogr. *20*, 79–83.

Toby, B.H. (2001). EXPGUI, a graphical user interface for GSAS. J. Appl. Crystallogr. *34*, 210–213.

Vakili, M., Deng, S., Cagnetta, G., Wang, W., Meng, P., Liu, D., and Yu, G. (2019). Regeneration of chitosan-based adsorbents used in heavy metal adsorption: a review. Separation Purif. Technology *224*, 373–387.

Wang, J., Lu, X.-G., Zhu, N., and Zheng, W. (2017). Thermodynamic and diffusion kinetic studies of the Fe-Co system. Calphad *58*, 82–100.

Wang, J., and Zhuang, S. (2017). Removal of various pollutants from water and wastewater by modified chitosan adsorbents. Crit. Rev. Environ. Sci. Technology *47*, 2331–2386.

Wang, W.-J., and Chen, Y.-W. (1991). Influence of metal loading on the reducibility and hydrogenation activity of cobalt/alumina catalysts. Appl. Catal. *77*, 223–233.

Wang, W., Jiang, X., Wang, X., and Song, C. (2018). FeCu bimetallic catalysts for selective CO_2 hydrogenation to olefin-rich C_{2+} hydrocarbons. Ind. Eng. Chem. Res. *57*, 4535–4542.

Wang, W., Wang, S., Ma, X., and Gong, J. (2011). Recent advances in catalytic hydrogenation of carbon dioxide. Chem. Soc. Rev. *40*, 3703–3727.

Wu, F.-C., Tseng, R.-L., and Juang, R.-S. (2010). A review and experimental verification of using chitosan and its derivatives as adsorbents for selected heavy metals. J. Environ. Manage. *91*, 798–806.

Yan, B., Zhao, B., Kattel, S., Wu, Q., Yao, S., Su, D., and Chen, J.G. (2019). Tuning CO2 hydrogenation selectivity via metal-oxide interfacial sites. J. Catal. *374*, 60–71.

Yang, H., Zhang, C., Gao, P., Wang, H., Li, X., Zhong, L., Wei, W., and Sun, Y. (2017). A review of the catalytic hydrogenation of carbon dioxide into value-added hydrocarbons. Catal. Sci. Technology *7*, 4580–4598.

Zhao, B., Sun, M., Chen, F., Shi, Y., Yu, Y., Li, X., and Zhang, B. (2021). Unveiling the activity origin of iron nitride as catalytic material for efficient hydrogenation of CO_2 to C_{2+} hydrocarbons. Angew. Chem. Int. Edition *60*, 4496–4500.

Zhao, J., and Friedrich, B. (2017). Synthesis of Gold Nanoparticles via the Chemical Reduction Methods (Shaker).

Zhu, Y., and Zaera, F. (2014). Selectivity in the catalytic hydrogenation of cinnamaldehyde promoted by Pt/SiO_2 as a function of metal nanoparticle size. Catal. Sci. Technology *4*, 955–962.

STAR★METHODS

KEY RESOURCES TABLE

REAGENT or RESOURCE	SOURCE	IDENTIFIER
Chemicals and reagents		
Acetic acid (≥99.7%)	Sigma-Aldrich	CAS: 64-19-7
Chitosan (low molecular weight)	Sigma-Aldrich	CAS: 9012-76-4
Sodium hydroxide (≥97.0%)	Sigma-Aldrich	CAS: 1310-73-2
Cobalt (II) chloride (≥99.9%)	Sigma-Aldrich	CAS: 7646-79-9
Iron (II) chloride (≥99.9%)	Sigma-Aldrich	CAS: 7758-94-3
Sodium borohydride (99.0%)	Sigma-Aldrich	CAS: 16,940-66-2

RESOURCE AVAILABILITY

Lead contact

Further information and requests for resources should be directed to and will be fulfilled by the lead contact, Hermenegildo García (hgarcia@upv.es).

Materials availability

This study did not generate new unique reagents.

Data and code availability

- All data reported in this paper will be shared by the lead contact upon request.
- This paper does not report original code.
- Any additional information required to reanalyze the data reported in this paper is available from the lead contact upon request.

METHOD DETAILS

Materials

Acetic acid (CH_3COOH), chitosan, sodium hydroxide (NaOH), cobalt (II) chloride ($CoCl_2$), iron (II) chloride ($FeCl_2$) and sodium borohydride ($NaBH_4$) were purchased from Sigma-Aldrich. All commercially available reagents were used without further purification and all aqueous solutions were prepared with MilliQ water.

Synthesis of Co-FeNPs@(N)G

Briefly, 400 mg chitosan and 250 μL acetic acid were added into 20 mL milli-Q water. After chitosan is dissolved completely, the solution was introduced dropwise, with a syringe (0.8 mm diameter needle), in an aqueous solution of sodium hydroxide (2 M, 500 mL). The gel microspheres were formed and immersed in NaOH solution for 2 h, then profusely washed with distilled water to pH = 7. The resulting hydrogel microspheres were washed by a series of ethanol/water baths with an increasing concentration of ethanol (10, 30, 50, 70, 90, 100 vol %, respectively) for 15 min in each and immersed in 40 mL $CoCl_2$-$FeCl_2$-ethanol solution with different concentration for 2 days with a slow stirring. After that, the microspheres were reduced with 150 mL of $NaBH_4$-ethanol solutions with different concentrations for 30 min and then exchanged by supercritical CO_2. The specific concentration and reduction time are shown in the following table. The resulting aerogel microspheres were pyrolyzed under Ar flow (200 mL/min), increasing the temperature at rate of 2°C/min up to 200°C for 2 h and then to 900°C for 2 h.

Table. List of samples under study

Samples	C_{Co} (mol/L)	C_{Fe} (mol/L)	C_{NaBH4} (mol/L)	Time (h)
1	0.001 × 0.79/0.21	0.001	0.05	5
2	0.002 × 0.79/0.21	0.002	0.05	5

(*Continued on next page*)

Continued

Samples	C_{Co} (mol/L)	C_{Fe} (mol/L)	C_{NaBH4} (mol/L)	Time (h)
3	0.003 × 0.79/0.21	0.003	0.05	5
4	0.003 × 0.79/0.21	0.003	0.05	12
5	0.003 × 0.79/0.21	0.002	0.1	5

Characterization of catalysts

Field Emission scanning electron microscopy (FESEM) images were acquired by using a JEOL JSM 6300 apparatus. HRTEM images were recorded in a JEOL JEM 2100F under an accelerating voltage of 200 kV. Samples were prepared by applying one drop of the suspended material in ethanol onto a carbon-coated nickel TEM grid and allowing them to dry at room temperature. Raman spectra were collected with a Horiba Jobin Yvon-Labram HR UV-visible-NIR (200-1600 nm) Raman Microscope Spectrometer using a 512 nm laser for excitation. The chemical composition of the samples was determined by combustion chemical analysis using a CHNS FISONS elemental analyser and by inductively coupled plasma apparatus with optical emission spectroscopy after dissolving completely Co and Fe metals of Co-FeNP@(N)G in *aqua regia* and analysis of the mother liquors. Powder diffraction patterns were recorded on a Shimadzu XRD-7000 diffractometer in Bragg-Brentano geometry with a CuK_{α} radiation source operated at 40 kV and 30 mA. Fresh and spent catalyst samples were investigated at room temperature in the 2θ interval 38 to 104° using a step scan program with a total duration of ~10 h (0.04°/step, counting time 22 s/step, sample spun at 15 rpm) to properly acquire diffraction patterns with sufficient resolution to characterize the phase composition of each sample.

Rietveld analysis of the experimental XRD patterns was performed using GSAS software (Larson and Von Dreele, 1994) with EXPGUI front end (Toby, 2001) compiled for GNU/Linux. Peak shapes were modeled as Thompson, Cox and Hastings pseudo-Voigt profile functions (Thompson et al., 1987).with Finger, Cox and Jephcoat correction for asymmetry due to axial divergence (Finger et al., 1994). Chebyshev polynomials fit was used for initial baseline extraction with subsequent refinement of the coefficients. Preferred orientation effects were modeled by the March-Dollase formalism (Dollase, 1986). Instrumental parameters (zero shift, initial peak profile) were determined from the refinement of a standard diffraction material (silicon powder, SRM 640days) recorded prior to the step-scanning measurements. Textural information (i.e. the extent of the coherently diffracting domains considered as average crystallite size and microstrain) were determined from the Rietveld refinement results (Balzar et al., 2004) considering the contribution of the pseudo-Voigt peak shape profile coefficients to the size and microstrain broadening after subtracting the instrumental broadening obtained from the measurement of the silicon powder standard.

Catalytic tests

Catalytic tests were performed in a fixed-bed plug flow reactor setup (PID Eng&Tech Microactivity Reference) equipped with a hotbox housing a stainless steel (SS316) straight tube reactor (Autoclave Engineers CNLX99012) heated by a low thermal inertia resistive oven. Temperature is measured with a fast response K-type thermocouple device inserted in the reactor body, in contact with the catalyst bed. Two calibrated mass flow controllers (Bronkhorst EL-FLOW) were used for the feed gases: a constant overall flow rate of 4 mL/min for several H_2:CO_2 molar ratios. The pressure was regulated at 10 bar with a system consisting of an exit needle valve actuated by a feedback-loop controlled servomechanism. For some experiments, water has been added through an HPLC pump (Gilson 307) to achieve a specific H_2:CO_2:H_2O molar ratio.

Analysis of the gaseous products was performed with an on-line coupled gas chromatograph (Agilent 7890A) using a sampling loop of 90 µL connected to a pneumatically actuated 6-way valve (Vici Valco). A PLOT column (Restek Rt-MSieve 5 Å, length 30 m) was used with H_2 carrier gas operated in constant pressure mode that generates linear velocities between 30 and 41 cm/s (temperature program: 20 min dwell at 35°C, 25°C/min. ramp, isothermal dwell at 260°C for 26 min), achieving thus a proper separation of the components. Detection was performed on a TC detector with H_2 reference gas.

For each catalyst, a series of isothermal measurements was recorded between 300 and 500°C with steps of 50°C; reactor effluent gas mixture was analyzed by GC at 90 min after setting each value of the reactor

temperature in order to achieve a steady operation regime (preliminary tests shown that after 35-50 min the values of the conversion/selectivity become constant).

Blank (i.e without catalyst) tests performed in the above-mentioned conditions generated negligible CO_2 conversion values: no detectable products under 350°C, 0.3% at 400°C, 1.9% at 450°C and 6% at 500°C, with selectivity of over 99% toward CH_4, CO being the only carbon-containing byproduct.

Theoretical calculations

Multipole Accelerated RI-J DFT calculations were performed using TURBOMOLE version 7.0 (Ahlrichs et al., 1989). Geometry optimizations and evaluation of energies were carried out applying the pure PBE functional (Perdew et al., 1996) at the def2-SVP level of theory. In addition, the Grimme's dispersion correction (Grimme et al., 2010) was also included as implemented in TURBOMOLE. The models used for this study contains 20 metallic atoms ($Co_{14}Fe_6$ cluster) following a random distribution and ending up with almost spherical geometry. MEP surfaces (isosurface 0.001 a.u.) of models were also computed at PBE-D3/def2-SVP level of theory by single-point calculations of the corresponding optimized structures using the Gaussian 16 package (Frisch et al., 2016).

Absorption (E_{ads}, eV) energies (E_{bind}, eV) were calculated as follows:

$$E_{ads} = E_{absorbate} - (E_{surface} + E_{CO2})$$

Where $E_{absorbate}$ are the energies of optimized systems in which CO_2 is covalently attached onto the metallic cluster; $E_{surface}$ corresponds to optimized structure of Co-Fe alloy cluster supported or not on graphene and $EECO_2$ is the energy of single CO_2 molecule.